HHS Public Access

Author manuscript

Acta Biomater. Author manuscript; available in PMC 2019 July 15.

Published in final edited form as:

Acta Biomater. 2018 July 15; 75: 323–333. doi:10.1016/j.actbio.2018.06.016.

Hyaluronic acid formulation of near infrared fluorophores optimizes surgical imaging in a prostate tumor xenograft

Joshua J. Souchek[a], **Nicholas E. Wojtynek**[b], **William M. Payne**[a], **Megan B. Holmes**[a], **Samikshan Dutta**[c], **Bowen Qi**[a], **Kaustubh Datta**[c], **Chad A. LaGrange**[d,e], and **Aaron M. Mohs**[a,c,e,*]

[a]Department of Pharmaceutical Sciences, University of Nebraska Medical Center, Omaha, Nebraska 68198, United States

[b]Eppley Institute for Research in Cancer and Allied Diseases, University of Nebraska Medical Center, Omaha, Nebraska 68198, United States

[c]Department of Biochemistry and Molecular Biology, University of Nebraska Medical Center, Omaha, Nebraska 68198, United States

[d]Department of Surgery, Division of Urologic Surgery, University of Nebraska Medical Center, Omaha, Nebraska 68198, United States

[e]Fred and Pamela Buffett Cancer Center, University of Nebraska Medical Center, Omaha, Nebraska 68198, United States

Abstract

The presence of positive surgical margins confers an increased risk of biochemical relapse and need for salvage therapy in men undergoing radical prostatectomy. Image-guided surgery using near-infrared (NIR) fluorescent contrast agents is a potential method to detect remaining cancerous tissue. The objective of this study was to evaluate three hyaluronic acid (HA) nanoparticle (NP) formulations loaded with NIR fluorophore for their ability to contrast-enhance prostate cancer. HA was modified by conjugation with the hydrophobic ligand, aminopropyl-1-pyrenebutanamide to drive nanoparticle self-assembly. Indocyanine green (ICG) was physicochemically entrapped in the HA-NP, termed NanoICG. Alternatively, Cy7.5 was directly conjugated to amphiphilic HA, termed NanoCy7.5. NanoCy7.5 was synthesized with two HA molecular weights to determine the HA size contribution to delivery to PC3 prostate tumor xenografts. Contrast-enhancement of the tumors and relative biodistribution were assessed by a series of fluorescence imaging, image-guided surgery with spectroscopy, and microscopic techniques. Intravenously administered NanoICG improved tumor signal-to-noise ratio (SNR) at 24 h over ICG by 2.9-fold. NanoCy7.5 with 10 kDa and 100 kDa HA improved tumor SNR by 6.6- and 3.1-fold over Cy7.5 alone, respectively. The PC3 xenograft was clearly identified with the image-guided system providing

*Corresponding author at: Department of Pharmaceutical Sciences, University of Nebraska Medical Center, Buffett Cancer Center, Room 5.12.315, Omaha, NE 68198, United States. aaron.mohs@unmc.edu (A.M. Mohs).

Disclosure

A.M.M. is a co-inventor of the image-guided surgery system used to detect NIR signal.

Appendix A. Supplementary data

Supplementary data associated with this article can be found, in the online version, at https://doi.org/10.1016/j.actbio.2018.06.016.

increased contrast enhancement compared to surrounding tissue for NanoICG and NanoCy7.5 with 10 kDa HA. NIR fluorescence microscopy showed that Cy7.5 in NPs with 10 kDa HA were distributed throughout the tumor, while NanoCy7.5 with 100 kDa HA or NanoICG delivered dye mainly to the edge of the tumor. CD31 staining suggested that PC3 tumors are poorly vascularized. These studies demonstrate the efficacy of a panel of HA-derived NPs in identifying prostate tumors *in vivo*, and suggest that by tuning the structural properties of these NPs, optimized delivery can be achieved to poorly vascularized tumors.

Statement of Significance

We have demonstrated the potential of a panel of near-infrared fluorescent (NIRF) nanoparticles (NPs) for image-guided surgery in a prostate cancer xenograft model. Image-guided surgery and imaging of organs *ex vivo* showed greater tumor signal and contrast when mice were administered NIRF dyes that were covalently conjugated to ($NanoCy7.5_{10k\text{-}PBA}$) or physicochemically entrapped in ($NanoICG_{PBA}$) hyaluronic acid (HA) NPs, compared to free dyes. These results show the potential to use these NPs as tools to detect the margins of tumors and to differentiate healthy and tumor tissue intraoperatively. Moreover, this project provides insight into selecting optimal formulation strategies for poorly vascularized tumors.

Keywords

Polymer conjugate; Self-assembly; Nanoparticle; Intraoperative imaging; ICG; Cy7.5

1. Introduction

Prostate cancer is the most diagnosed cancer in men, accounting for almost 1 in 5 new cancer diagnoses, and is the third leading cause of death resulting from cancer in men in the United States [1]. Nearly 80% of new prostate cancer diagnoses have localized disease [1], with the most common interventions being surgery, radiotherapy, and monitoring or surveillance. Population-based data sets show that 40–50% of newly diagnosed men with localized disease undergo radical prostatectomy [2,3], making it the most common treatment in this setting. However, treatment for prostate cancer can have adverse effects on urinary, bowel, or sexual function.

Up to 40% of men have biochemical recurrence after radical prostatectomy upon 10–15 year follow-up [4]. In one study, over 30% of men undergoing open radical prostatectomy had positive margins, and the presence of a positive margin was associated with increased risk of biochemical recurrence, local recurrence, and need for salvage therapy [5]. Surgery for prostate cancer has evolved, with open radical prostatectomy being largely replaced with robot-assisted radical prostatectomy (RARP) [6], with numbers of RARPs increasing from 1.8% to 85% in the United States during the period of 2003–13 [7]. A meta-analysis reported that positive surgical margins for RARPs ranged from 6.5% to 32% (mean 15%) [8]. Positive surgical margin rates for RARPs have been reported to be at least equivalent to radical retropubic prostatectomy in a meta-analysis [9], and a randomized, controlled phase 3 study showed no statistically significant difference in positive surgical margin rates between radical retropubic prostatectomy vs RARP [10].

Fluorescence image-guided surgery (FIGS) has the potential to differentiate normal versus diseased tissue and provide real-time guidance for pathology on resected specimens. FIGS approaches often make use of the “NIR window”, which allows for imaging in wavelengths of approximately 700–1000 nm, where light has its maximum depth of penetration in tissue due to relatively lower tissue absorption of light by water and hemoglobin [11]. The FDA- and EMA-approved NIR fluorophore, indocyanine green (ICG), has been used in tens of thousands of patients with low side effect rate (<0.15%) [12]. ICG primarily reflects initial vascular distribution (through binding to albumin and other plasma proteins) and subsequent hepatobiliary excretion, and thus has been used for tests of cardiac output, hepatic function and liver blood flow, as well as ophthalmic angiography [12].

Fluorescence imaging has also been demonstrated clinically during cancer surgery for a number of cancer types, utilizing fluorophores such as ICG, methylene blue, and 5-aminolevulinic acid [13]. Fluorescence-enhanced RARP using ICG injection directly into the prostate of patients has been performed for sentinel lymph node mapping [14–16]. Further, direct injection of multimodal ICG-^{99m}Tc-NanoColl into the prostate was used for sentinel lymph node mapping [17]. These studies showed fluorescence surgery to be feasible and safe, but displayed variable levels of specificity and sensitivity for detection of nodal metastasis.

Targeted NIR dyes and nanoparticles (NPs) are being developed as novel contrast agents for IGS. Several types of fluorescent NPs have been developed for cell imaging and biomedical applications [18,19]. Fluorescent NPs take advantage of the enhanced permeability and retention (EPR) effect of tumors, can be specifically targeted to tumors, and can be modified to avoid clearance [20]. In this study we assessed the delivery of NIR dyes using hyaluronic acid (HA)-based NPs. HA is a glycosaminoglycan found throughout the body, can have a variety of sizes composed of repeat units of β(1,4) D-glucuronic acid and β(1,3)N-acetyl-D-glucosamine, and is capable of binding to a number of receptors, including CD44, LYVE1, and Stabilin-2 (HARE) [21,22]. With its biocompatible, non-immunogenic characteristics, and potential to target overex-pressed CD44 on some tumors or accumulate passively by EPR, HA has been used in synthesis of a number of NPs for imaging and drug delivery applications [23–28]. A common method of NP formulation is to modify the hydrophilic HA backbone with hydrophobic ligands to drive self-assembly [29–31].

In this study, we report the *in vivo* imaging evaluation of a panel of three HA-derived near-infrared fluorescent (NIRF) NPs that used physicochemically entrapped ICG or covalently conjugated Cy7.5. The “NanoICG” formulation used 10 kDa HA polymers and the “NanoCy7.5” formulation used 10 kDa and 100 kDa HA polymers. The NPs were delivered to nude mice bearing PC3 tumors and examined at 24 h. Image-guided surgery, tumor contrast, biodistribution, and distribution through tumors were analyzed.

2. Materials and methods

2.1. Materials

Sodium hyaluronate (10 kDa and 100 kDa) was purchased from Lifecore Biomedical (Chaska, MN, USA). 1-Pyrenebutyric acid, 1,3-diaminopropane, and ICG was obtained

from Sigma-Aldrich (St. Louis, MO, USA). Cy7.5-amine was purchased from Lumiprobe Corporation (Hallandale Beach, FL, USA). 1-ethyl-3-(3-dimethylaminopropyl) carbodiimide (EDC), N-hydroxysuccinimide (NHS), N,N-dimethylformamide (DMF), dimethyl sulfoxide (DMSO), methanol, and dialysis membranes (3500 MWCO and 6000–8000 MWCO), were purchased from Thermo Fisher Scientific (Waltham, MA, USA). Ethanol was purchased from the Warner-Graham Company (Cockeysville, MD, USA) or the General Supply at the University of Nebraska Medical Center. Desalting PD10 columns were purchased from GE Health-care Bio-Sciences (Pittsburgh, PA, USA). D_2O [99.9% D] and DMSO-D_6 [99.8% D] were purchased from EMD Millipore. All water was obtained from a Barnstead NANOpure Diamond or Barnstead GenPure system (Thermo Fisher Scientific) producing 18.2 MX water.

2.2. Cell lines and culture

PC3 prostate cancer cell lines were obtained from the American Type Culture Collection (Manassas, VA, USA). PC3 cells were maintained in RPMI 1640 medium supplemented with 10% fetal bovine serum, 100 I.U. penicillin, and 100 μg/mL streptomycin. Cells were incubated at 37 °C in a humidified incubator with 5% CO_2.

2.3. Preparation of HA-PBA nanoparticles

Synthesis of HA nanoparticles (NPs) was performed as described previously [29]. Briefly, aminopropyl-1-pyrenebutanamide (PBA) was synthesized from 1-pyrenebutyric acid by refluxing in methanol at 60 °C for 6 h, followed by purification and refluxing in 1,3-diaminopropane at 135 °C for six h. HA-PBA conjugates were synthesized with 10 kDa or 100 kDa HA polymers conjugated with 10 wt% PBA by first dissolving HA in 50:50 H_2O:DMF containing 10-fold molar excess of EDC/NHS, followed by dropwise addition of PBA in DMF and stirring for 24 h. Each polymer conjugate was purified by dialysis (3500 Da MWCO, Fisher Scientific) in 50:50 H_2O:EtOH for 24 h followed by dialysis in pure H_2O for an additional 48 h. Cy7.5-amine was conjugated to HA-PBA using NHS/EDC chemistry [30], while ICG was physically loaded as described previously (Fig. 1) [29]. The reaction mixture was placed in a dialysis bag with MWCO of 3500 (10 kDa HA-PBA derivatives) or 6000–8000 Da (100 kDa HA-PBA derivatives) and dialyzed against water for 24 h with 4–6 water changes. Residual unconjugated Cy7.5 dye was removed from the HA-conjugates via PD10 desalting columns with ultrapure water as a mobile phase. NPs were then frozen, lyophilized, and stored at −20 °C.

2.4. Nanoparticle characterization

The hydrodynamic diameter (HD) and zeta potential of the NPs dissolved in water and filtered in a 0.45 μm syringe filter was determined on a ZetaSizer NanoZS90 (Malvern Instruments; Malvern, UK). Fluorophore-loading content was determined with UV–Vis spectroscopy after disassembly of NPs in 1:1 H_2O:DMSO using an Evolution 220 spectrophotometer (Thermo Fisher Scientific, Madison, WI, USA) with a standard curve of ICG or Cy7.5 in 1:1 H2O/DMSO. HA_{10k}-PBA conjugates loaded with ICG are termed $NanoICG_{PBA}$. NanoCy7.5 conjugates composed of 10 kDa HA with PBA are identified as $NanoCy7.5_{10k\text{-}PBA}$, while those composed of 100 kDa HA with PBA are identified as $NanoCy7.5_{100k\text{-}PBA}$. ICG and Cy7.5 were chosen for their optimized fluorescence in the

near infrared window, which minimizes tissue scatter and absorbance [11], and has optimized integration with near infrared imaging systems (Fig. 1C).

Size exclusion chromatography was performed using a Waters 1515 HPLC pump equipped with Waters Ultrahydrogel 1000 and 250 columns, a Waters 2998 photodiode array detector, a Waters 2414 refractive index detector (Waters Corporation; Milford, MA), and a Wyatt miniDAWN TREOS multi-angle light scattering detector (Wyatt Technology Corporation; Santa Barbara, CA). Data were analyzed using Astra 6.1.7 (Wyatt Technology Corporation; Santa Barbara, CA). Samples were prepared at a concentration of 4.0 mg/mL using two mobile phases; an aqueous 0.1 M phosphate buffer at pH 7.0, or for the disassembly buffer, a solution of 50% DMSO in 0.1 M aqueous phosphate buffer at pH 7.0 (Fig. 2).

NanoCy7.5$_{10k\text{-}PBA}$ and NanoCy7.5 $_{100k\text{-}PBA}$ NPs were analyzed on a Bruker Avance 500 MHz NMR spectrometer using a 5 mm probe at room temperature. NanoCy7.5$_{10k\text{-}PBA}$ and NanoCy7.5$_{100k\text{-}PBA}$ NPs were analyzed in 50/50 D_2O/DMSO-D_6. ^1H NMR of HA-PBA is provided in our previous publication [29]. Transmission electron microscope (TEM) images were obtained using a FEI Tecnai G2 Spirit TEM (FEI; Hillsboro, Oregon) available in UNMC's electron microscopy core facility. Prior to TEM imaging, NPs (concentration 1.0 mg/mL in PBS) were placed on a formvar/silicone monoxide-coated 200 mesh copper grid and allowed to adhere for approximately 5 min, NanoVan negative stain was applied for 30 s, and the sample was blotted to remove excess solvent or material. TEM images of NanoICG and NanoCy7.5$_{10k\text{-}PBA}$ NPs are also provided in our previous publications [23,32,33]. The stability of NanoICG$_{PBA}$ in a solution of PBS containing bovine serum albumin (BSA) has been reported [23], showing that ICG was rapidly released into albumin-containing solution across a dialysis membrane. It was also shown that a NanoCy7.5 variant with aminopropyl-5β-cholanamide as the conjugated hydrophobic moiety, NanoCy7.5$_{100k\text{-}5\beta CA}$, showed limited disassembly into albumin-containing solution over a 6 h period, and then gradual disassembly over the next 72 h [23]. The cell cytotoxicity of NanoICG$_{PBA}$ was previously shown to be negligible in cultured cells [29], as was also reported for NanoCy7.5$_{10k\text{-}PBA}$ [33].

Fluorescent stability of the NPs was studied in phosphate-buffered solutions under different pH, adjusting the pH to 4, 5, 6, 7, and 8 by mixing solutions of disodium phosphate, monosodium phosphate, and phosphoric acid, while keeping the ionic strength constant. Samples were first dissolved to a dye (Cy7.5 or ICG) concentration of 100 μM in each pH solution, then further diluted to a dye concentration of 10 μM and incubated for 1 h. After incubation, the NPs were disassembled by adding DMSO (50/50 buffer:DMSO final) to have a final dye concentration of 5 μM, and absorbance and fluorescence readings were taken. Spectral acquisition after disassembly in DMSO was chosen since previous reports show that NP assembly in H_2O can quench ICG and Cy7.5 fluorescence [29,30]. Fluorescence spectra were obtained on a FluoroMax-4 spectrofluorometer equipped with a NIR extended range PMT (Horiba Jobin Yvon; Edison, NJ, USA) with excitation wavelength of 785 nm and emission wavelength range from 800 to 900 nm. NanoCy7.5$_{100k\text{-}PBA}$ has lower solubility and was diluted to same final concentration. As controls, NPs were dissolved directly in 50/50 buffer:DMSO solutions (pH adjusted) to a final dye concentration of 5 μM, and absorbance and fluorescence readings were taken.

2.5. Tumor implantation

All animal work was performed under an approved protocol by the University of Nebraska Medical Center Institutional Animal Care and Use Committee (IACUC). PC3 cells (3×10^6 cells) suspended in 100 μL of 1:1 media:matrigel (matrigel #354234 from Corning, Corning, NY, USA) were injected subcutaneously on the flank of 4–5 week old male athymic nude mice (Strain: J:NU, Jackson Laboratory, Bar Harbor, ME, USA). Tumors were allowed to grow at least three weeks.

2.6. Near-infrared fluorescent contrast agent delivery, image-guided surgery, and relative organ distribution

When the tumors reached over 150 mm^3, mice were injected intravenously (200 μL) via the tail vein with either ICG, $NanoICG_{PBA}$, Cy7.5-amine, $NanoCy7.5_{10k\text{-}PBA}$, or $NanoCy7.5_{100k\text{-}PBA}$. The quantity of ICG was equal across both ICG and $NanoICG_{PBA}$ (10 nmol [7.75 μg] ICG/mouse), and the quantity of Cy7.5 was equal across Cy7.5-amine, $NanoCy7.5_{10k\text{-}PBA}$, and $NanoCy7.5_{100k\text{-}PBA}$ (1.2 nmol [984 ng] Cy7.5/mouse). Mice were euthanized 24 h after injection. A simulated image-guided surgery was performed using a custom designed image-guided surgery system that integrates local NIR spectroscopy and wide-field imaging [34]. With this system, the contrast enhancement of tumor relative to surrounding tissues was determined by taking snapshots and videos. Necropsied tissue was subjected to additional spectroscopic analysis. Spectra from tissues were obtained with the tip of the laser 1 cm from the tissue surface, with laser power at 30 mW or 80 mW, and results were normalized, which is consistent with our previously reported methods [23,29,32,34].

After necropsy, mouse organs were imaged using a Pearl Trilogy Small Animal fluorescence imaging system (LI-COR; Lincoln, NE, USA) to detect ICG or Cy7.5 (800 nm channel). Images were analyzed with LI-COR Image Studio 5.0 software to manually draw areas of interest around tumors and organs, and average pixel intensity was used to calculate signal to noise ratio (SNR). SNR = (average tissue intensity per pixel in an area of interest)/(standard deviation of background area of interest).

2.7. Histological analysis and fluorescence microscopy

Tumor tissue from image-guided surgery studies was immediately placed in O.C.T. embedding media gel (Fisher Healthcare) and rapidly frozen in liquid nitrogen. These samples were then cut and processed by the UNMC Tissue Sciences Facility. Sections from each sample were stained with hematoxylin and eosin (H&E) or were left unstained for NIR fluorescence microscopy. Representative tumor sections were also stained with Masson's trichrome stain or antibodies, including anti-mCD31, endothelial marker (1:100, ab28364 Abcam, Cambridge, MA, USA); anti-hKi67, proliferation marker (1:200, ab16667 Abcam); and anti-hCD44 (1:500, #3570 Cell Signaling Technology, Danvers, MA, USA), a cell surface receptor for HA. Images were taken with an Olympus (Tokyo, Japan) IX73 inverted microscope with a xenon excitation source and imaged with an Olympus DP80 Digital Camera and cellSens Dimension software. Unstained slides were imaged for autofluorescence with a FITC filter cube, and NIR fluorescence with an ICG filter cube that

was capable of imaging both ICG and Cy7.5 fluorescence emission. Micrographs were further analyzed with Image J (NIH) using identical processing parameters.

2.8. Statistical analysis

Data was analyzed in Prism 7 software (Graphpad, La Jolla, CA, USA). Biodistribution of NanoCy conjugates in organs were analyzed using 2-way ANOVA with Tukey's multiple comparisons test; SNR comparison in tumors were analyzed using a 1-way ANOVA and Tukey's multiple comparisons test; biodistribution for NanoICG was analyzed using multiple t tests. Statistical tests are mentioned in the figure captions. All data is shown as mean ± standard deviation (SD).

3. Results

3.1. Nanoparticle characterization

HA was conjugated to PBA or PBA and Cy7.5. PBA conjugation was confirmed by ^{1}H NMR as previously reported for 10 kDa HA [29], while ^{1}H NMR of the 10 and 100 kDa HA conjugates with PBA and Cy7.5 is reported in Supplementary Fig. 1 and is characterized by the presence of the aromatic pyrene group, the piconjugated system on the Cy7.5 moiety, and the N-acetyl methyl group on HA. NanoCy7.5$_{10k\text{-}PBA}$ had a hydrodynamic diameter (HD) of 195 ± 13 nm with a PDI of 0.431 ± 0.116, and zeta potential of −18.5 ± 0.9 mV. NanoCy7.5$_{100k\text{-}PBA}$ had an HD of 144 ± 4 nm with a PDI of 0.174 ± 0.052, and zeta potential of −13.2 ± 2.1 mV. The relatively smaller HD of NanoCy7.5$_{100k\text{-}PBA}$ compared to NanoCy7.5$_{10k\text{-}PBA}$ is likely due to the higher degree of Cy7.5 conjugation, which promotes greater packing of NanoCy7.5$_{100k\text{-}PBA}$ in aqueous conditions, and is consistent with our previous results [30]. TEM images similarly showed NanoCy7.5$_{100k\text{-}PBA}$ to be smaller than NanoCy7.5$_{10k\text{-}PBA}$ (Supplementary Fig. 2). NanoICG$_{PBA}$ had a HD of 84 ± 11 nm with a PDI of 0.244 ± 0.016. The final weight percent of Cy7.5 was 1.4 wt% for NanoCy7.5$_{10k\text{-}PBA}$, and 11.2 wt% for NanoCy7.5$_{100k\text{-}PBA}$. The final weight percent of ICG was previously reported to be 9.4 wt% in NanoICG$_{PBA}$ [29].

Size exclusion chromatography of unmodified HA, HA$_{10k}$-PBA and disassembled NanoCy7.5$_{10k\text{-}PBA}$ showed a difference in size between the three samples of 10 kDa HA, with NanoCy7.5$_{10k\text{-}PBA}$ eluting sooner (Fig. 2A). When compared to Fig. 2B, which demonstrates the SEC profile of assembled conjugates, the samples in Fig. 2B appear slightly larger (i.e., elute sooner) due to associations between polymer strands forming self-assembled NPs. The same trend is observed for the 100 kDa HA samples, in which the assembled (Fig. 2D) samples are slightly larger than the disassembled (Fig. 2C) samples.

NPs showed high fluorescence stability at biological pH, with NanoCy7.5$_{100k\text{-}PBA}$ showing decreased fluorescence at high (pH 8) and low (pH 4) pH (Supplementary Fig. 3). A broadening of the absorbance spectra was also seen for NanoCy7.5$_{100k\text{-}PBA}$ at pH 8, possibly due to scattering and a decreased Cy7.5 solubility at higher pH (Supplementary Fig. 4).

3.2. Relative biodistribution

The relative biodistribution of the NIRF NP formulations and free dyes was assessed using the LI-COR Pearl Trilogy imaging system. Representative images of tissues harvested 24 h after intravenous administration are shown in Fig. 3A–C, E, and F. The fluorescence intensity of organs was quantified for all mice as the signal-to-noise ratio (SNR) values and were corrected for area (Fig. 3D and G). Overall fluorescence signal, including that emitting from the PC3 tumors, was higher with Cy7.5-based agents compared to ICG-based NPs (Fig. 3D, G, and H). The highest SNRs were observed in the liver and spleen for NanoCy7.5$_{10k\text{-}PBA}$ and NanoCy7.5$_{100k\text{-}PBA}$, followed by the kidney, while the highest SNRs were from liver and kidney for Cy7.5, ICG, and NanoICG$_{PBA.}$ NanoCy7.5$_{100k\text{-}PBA}$ showed very high signal in the spleen (3.2-fold higher than NanoCy7.5$_{10k\text{-}PBA}$), consistent with previous studies using 100 kDa HA-derived NPs in breast cancer models [23]. NPs derived from Cy7.5, which was covalently-bound to HA, increased delivery to PC3 tumors. Administration of NanoCy7.5$_{10k\text{-}PBA}$ resulted in a 6.6-fold increase in tumor signal compared to Cy7.5-amine. NanoCy7.5$_{100k\text{-}PBA}$ had a 3.1-fold higher signal compared to Cy7.5-amine, but interestingly had a lower signal than NanoCy7.5$_{10k\text{-}PBA}$. NanoICG$_{PBA}$ displayed a 2.9-fold higher NIR signal compared to free ICG in PC3 tumors (Fig. 3H).

To examine the image contrast and change in biodistribution of NIR signal provided by NPs, the SNR of tumor was compared to surrounding muscle and high background tissues. The tumor-to-muscle ratio for NanoCy7.5$_{10k\text{-}PBA}$ was significantly higher when compared to Cy7.5-amine (3.0-fold, Fig. 4A), while the tumor-to-kidney ratio for NanoCy7.5$_{10k\text{-}PBA}$ was significantly higher than Cy7.5-amine (5.4-fold), NanoCy7.5$_{100k\text{-}PBA}$ (1.9-fold), and ICG(2.4-fold) (Fig. 4C). Compared to ICG, NanoICG$_{PBA}$ had significantly increased tumor-to-muscle (2.2-fold), tumor-to-kidney (2.3-fold), and tumor-to-spleen ratios (1.7-fold) (Fig. 4A, C, and D). NanoICG$_{PBA}$ also displayed significantly higher tumor-to-liver and tumor-to-spleen ratios compared to all Cy7.5 agents, and had increased tumor-to-muscle and tumor-to-kidney ratio compared to Cy7.5-amine and NanoCy7.5$_{100k\text{-}PBA}$ (Fig. 4A–D).

3.3. Image-guided surgery

NanoICG$_{PBA}$, NanoCy7.5$_{10k\text{-}PBA}$, or NanoCy7.5$_{100k\text{-}PBA}$ and their respective dye-alone controls were examined for use in image-guided surgery. Intraoperative imaging provided by FIGS showed that NIR fluorescence could be detected in subcutaneous PC3 tumors during surgery for mice administered NanoCy7.5$_{10k\text{-}PBA}$ (1.2 nmol Cy7.5/mouse), while adjacent muscle had minimal enhancement (Fig. 5A). Keeping the wide-field imaging parameters constant, NanoCy7.5$_{100k\text{-}PBA}$ was readily detected in tumor with 80 mW excitation power but could also be seen in adjacent areas of muscle around the tumor. NanoICG$_{PBA}$ (10 nmol/mouse) was seen in the tumor, but with less intensity using 80 mW excitation power, and was not seen in adjacent muscle tissue. Cy7.5-amine and ICG controls at the same excitation power and wide-field imaging parameters, resulted in no or minimal detection of tumor during surgery (Fig. 5A). NIR fluorescence was observed in the gut area for all contrast agents.

Spectroscopic analysis indicated stronger NIR fluorescence in the excised tumor compared to excised muscle (i.e. quadriceps femoris muscle) for all contrast agents (Fig. 5B and C),

with ICG and NanoICG$_{PBA}$ having statistically higher levels in tumor, and NanoCy7.5$_{10k\text{-}PBA}$ approaching significance ($p = 0.08$). Higher AUC was seen in tumors of mice injected with NanoICG$_{PBA}$ compared to ICG (1.6-fold) but was not statistically significant. Higher AUC was seen in tumors of mice injected with NanoCy7.5$_{10k\text{-}PBA}$ and NanoCy7.5$_{100k\text{-}PBA}$ compared to Cy7.5-amine (2.2-fold and 2.5-fold, respectively), with NanoCy7.5$_{100k\text{-}PBA}$ achieving significance.

3.4. Distribution of IR dyes within tumors

Histological analysis of PC3 tumors was used to determine the distribution of IR dyes throughout the tumor. NIR fluorescence microscopy showed that NanoCy7.5$_{10k\text{-}PBA}$ was distributed throughout the entire tumor, while NIR signal from NanoCy7.5$_{100\text{-}k\text{-}PBA}$ and NanoICG$_{PBA}$ was seen mainly at the edge of the tumor with a few areas of signal within the tumor (Fig. 6A). CD31 staining showed that PC3 tumors are poorly vascularized. Staining of PC3 tumors with anti-hKi67 showed that proliferating cancer cells were distributed throughout the tumor, with approximately 30–40% of tumor cells staining positive for Ki67. Masson's tri-chrome staining showed low collagen levels within the tumor, with increased levels toward the tumor periphery. Tumor cells were highly positive for CD44 expression (Fig. 6B), a protein known to bind HA [35].

4. Discussion

We synthesized three NP formulations derived from HA, based on methods that we have previously described [23,29,30], to assess delivery of the NIR fluorophores Cy7.5 and ICG in a xenograft model of prostate cancer. Our previous studies have used PBA as a hydrophobic ligand conjugated to HA to drive self-assembly into NPs for NIR dye loading. We also recently reported the use of HAPBA NPs loaded with the weight loss drug and fatty acid synthase (FASN) inhibitor, orlistat, for treatment of breast cancer and taxane-resistant prostate cancer cell lines in culture [24,31]. Thus, the previous and current imaging studies predict that PBA-HA NPs will enhance delivery of dyes and hydrophobic drugs to tumors *in vivo*.

Though ICG and NanoICG$_{PBA}$ were administered at a higher dose (10 nmol of ICG/ mouse) compared to Cy7.5 formulations (1.2 nmol of Cy7.5/ mouse), the Cy7.5 formulations showed higher SNR in all tissues 24 h after administration (Fig. 3). This is due, in part, to Cy7.5 having a higher quantum yield compared to ICG, and because Cy7.5 was directly conjugated to HA, while ICG was only physically entrapped. Expectedly, our previous studies showed slower *in vitro* release/disassembly of Cy7.5 from NanoCy7.5 formulations compared to ICG from NanoICG [23]. Nonetheless, NanoICG$_{PBA}$ had the highest tumor-to-muscle, tumor-to-liver, and tumor-to-spleen ratios compared to the other NPs tested, and the second highest tumor-to-kidney ratio (Fig. 4). Thus, even though Cy7.5 was brighter than ICG, NPs derived using ICG resulted in higher contrast in some cases. NanoCy7.5$_{10k\text{-}PBA}$ had the highest SNR in tumors compared to all the agents tested (Fig. 3H), and had significantly increased tumor-to-muscle ratio compared to free Cy7.5-amine (Fig. 4A). NanoCy7.5$_{10k\text{-}PBA}$ also had high signal in the tumor during FIGS (Fig. 5), and the spectral AUC trended to, but did not achieve significance compared to muscle (Fig. 5C). These

results suggest that NPs with 10 kDa HA provided an advantage to delivery of ICG and Cy7.5 to PC3 tumors.

In the current work, NanoICG$_{PBA}$ had significantly increased tumor-to-muscle SNR (2.2-fold) at 24 h. In breast cancer tumors, NanoICG$_{PBA}$ had 2.3-fold increased tumor-to-muscle contrast-to-noise ratio (CNR) in MDA-MB-231 tumors [29] and nearly 2.2-fold increased tumor-to-muscle CNR in 4T1 tumors at 24 h [23]. In pancreatic tumors, NanoICG$_{PBA}$ signal was 2.0 times that of the ICG group [32]. Thus, the contrast ratios compared to muscle are consistently about 2-fold higher for NanoICG$_{PBA}$. However, tumor SNR values in the current study were much less for NanoICG$_{PBA}$ in PC3 prostate tumors compared to our previous studies. PC3 xenograft tumors have been shown to have less vasculature as assessed by CD31 staining compared to other prostate cancer xenografts [36], which was confirmed by low CD31 staining (Fig. 6B). The low vessel staining together with high proliferative staining (Ki67, Fig. 5B) may be a contributing factor why SNR values were less, since others have shown that proliferating cancer cells cause intratumoral vessels to compress and collapse [39].

It was surprising that NanoCy7.5$_{10k\text{-}PBA}$ had significantly higher SNR compared to NanoCy7.5$_{100k\text{-}PBA}$ in PC3 tumors (Fig. 3D and H), since 100 kDa HA NPs showed higher SNR in breast cancer tumors [23], and 100 kDa HA NPs showed more specific binding to CD44-expressing cells compared to 10 kDa HA NPs using an *in vitro* inhibition assay [30]. Others have shown that high MW HA forms tighter, multivalent interactions with CD44 [37], which is highly expressed in PC3 cells [38], and confirmed here in Fig. 6B. The higher SNR of NanoCy7.5$_{10k\text{-}PBA}$ could be explained by several potential reasons. First, NanoCy7.5$_{100k\text{-}PBA}$ showed very high SNR in the spleen (3.2-fold higher than NanoCy7.5$_{10k\text{-}PBA}$), consistent with previous studies using 100 kDa HA-derived NPs in breast cancer models [23]. This preferential accumulation in the spleen could limit the amount of NanoCy7.5$_{100k\text{-}PBA}$ available to the tumor. Further, the differences in tumor distribution could be due to penetration behavior. To that end, once the NPs studied here escape from the vasculature due to leaky vessels, it is possible that the NPs are limited in their diffusion based on the MW of the HA backbone [23].

In summary, we observed that even though HA-based NPs were taken up by PC3 tumors, they do not enhance tumors uniformly, nor do they enhance across tumors evenly (summarized in Fig. 7 and Table 1). For image-guided surgery applications, where the margins/surface of the tumor are important to be seen, expression of CD44 may be important for HA-based NP binding but did not seem to play a role for distribution through the tumor. Future studies are required to assess NIR signal correlation with CD44 expression of tumor cells or other markers of macrophages and stromal cells to determine why NanoCy7.5$_{10k\text{-}PBA}$ had higher SNR compared to NanoCy7.5$_{100k\text{-}PBA}$. Future studies will assess the delivery of NIRF NPs in more dynamic tumor models, including orthotopic tumor models. Future studies will also assess the uptake of NIR dye in the normal prostate, the bladder or seminal vesicles, which are important background tissues during prostate surgery.

5. Conclusion

We have demonstrated the potential of a panel of NIRF NPs for image-guided surgery in a prostate cancer model. Mock image-guided surgery and imaging of organs *ex vivo* showed greater tumor signal and contrast when mice were administered NIRF dyes that were covalently conjugated to (i.e., NanoCy7.5$_{10k\text{-}PBA}$) or physicochemically entrapped in (i.e., NanoICG$_{PBA}$) HA NPs. These results show the potential to use these NPs as tools to detect the margins of tumors and to differentiate healthy and tumor tissue intraoperatively. NPs with dyes that were chemically conjugated to HA had higher tumor signal compared to those that physico-chemically entrapped dyes, indicating that a lengthened stability profile allowed the NPs to have higher accumulation, either by passive accumulation or active targeting by HA-binding proteins. Future efficacy studies are needed to examine the effect on recurrence and survival after tumor removal using these contrast agents.

Supplementary Material

Refer to Web version on PubMed Central for supplementary material.

Acknowledgements

We thank Dr. Jiang Jiang and Lijun Sun for technical assistance in the UNMC Tissue Science Facility. This work was funded by the National Institute of General Medical Sciences (P20 GM103480), the National Institute of Biomedical Imaging and Bio-engineering (R01 EB019449), the Fred & Pamela Buffett Cancer Center at UNMC (P30 CA036727), Davies Philanthropy, and the Nebraska Research Initiative.

Abbreviations:

AUC	Area under the curve
FIGS	fluorescence image-guided surgery
ICG	indocyanine green
IGS	image-guided surgery
HA	hyaluronic acid
NIR	near-infrared
NIRF	near-infrared fluorescent
NP(s)	nanoparticle(s)
PBA	aminopropyl-1-pyrenebutanamide
RARP	robot-assisted radical prostatectomy

References

[1]. Siegel RL, Miller KD, Jemal A, Cancer Statistics, 2017, CA Cancer J. Clin 67 (2017) 7–30, 10.3322/caac.21387. [PubMed: 28055103]

[2]. Cooperberg MR, Broering JM, Carroll PR, Time trends and local variation in primary treatment of localized prostate cancer, J. Clin. Oncol 28 (2010) 1117–1123, 10.1200/JCO.2009.26.0133. [PubMed: 20124165]

[3]. Abdollah F, Sun M, Thuret R, Jeldres C, Tian Z, Briganti A, Shariat SF, Perrotte P, Rigatti P, Montorsi F, Karakiewicz PI, A competing-risks analysis of survival after alternative treatment modalities for prostate cancer patients: 1988–2006, Eur. Urol 59 (2011) 88–95, 10.1016/j.eururo.2010.10.003. [PubMed: 20965646]

[4]. Boorjian SA, Eastham JA, Graefen M, Guillonneau B, Karnes RJ, Moul JW, Schaeffer EM, Stief C, Zorn KC, A critical analysis of the long-term impact of radical prostatectomy on cancer control and function outcomes, Eur. Urol 61 (2012) 664–675, 10.1016/j.eururo.2011.11.053. [PubMed: 22169079]

[5]. Boorjian SA, Karnes RJ, Crispen PL, Carlson RE, Rangel LJ, Bergstralh EJ, Blute ML, The impact of positive surgical margins on mortality following radical prostatectomy during the prostate specific antigen era, J. Urol 183 (2010) 1003–1009, 10.1016/j.juro.2009.11.039. [PubMed: 20092854]

[6]. Litwin MS, Tan H-J, The diagnosis and treatment of prostate cancer, JAMA 317 (2017) 2532–2542, 10.1001/jama.2017.7248. [PubMed: 28655021]

[7]. Lancet The, Robotic surgery evaluation: 10 years too late, Lancet 388 (2016) 1026 10.1016/S0140-6736(16)31586-0.

[8]. Novara G, Ficarra V, Mocellin S, Ahlering TE, Carroll PR, Graefen M, Guazzoni G, Menon M, Patel VR, Shariat SF, Tewari AK, Van Poppel H, Zattoni F, Montorsi F, Mottrie A, Rosen RC, Wilson TG, Systematic review and meta-analysis of studies reporting oncologic outcome after robot-assisted radical prostatectomy, Eur. Urol 62 (2012) 382–404, 10.1016/j.eururo.2012.05.047. [PubMed: 22749851]

[9]. Tewari A, Sooriakumaran P, Bloch DA, Seshadri-Kreaden U, Hebert AE, Wiklund P, Positive surgical margin and perioperative complication rates of primary surgical treatments for prostate cancer: A systematic review and meta-analysis comparing retropubic, laparoscopic, and robotic prostatectomy, Eur. Urol 62 (2012) 1–15, 10.1016/j.eururo.2012.02.029. [PubMed: 22405509]

[10]. Yaxley JW, Coughlin GD, Chambers SK, Occhipinti S, Samaratunga H, Zajdlewicz L, Dunglison N, Carter R, Williams S, Payton DJ, Perry-Keene J, Lavin MF, Gardiner RA, Robot-assisted laparoscopic prostatectomy versus open radical retropubic prostatectomy: early outcomes from a randomised controlled phase 3 study, Lancet 388 (2016) 1057–1066, 10.1016/S0140-6736(16)30592-X. [PubMed: 27474375]

[11]. Weissleder R, A clearer vision for in vivo imaging, Nat. Biotechnol 19 (2001) 316–317, 10.1038/86684. [PubMed: 11283581]

[12]. Hope-Ross M, Yannuzzi LA, Gragoudas ES, Guyer DR, Slakter JS, Sorenson JA, Krupsky S, Orlock DA, Puliafito CA, Adverse reactions due to indocyanine green, Ophthalmology 101 (1994) 529–533, 10.1016/S0161-6420(94)31303-0. [PubMed: 8127574]

[13]. Vahrmeijer AL, Hutteman M, van der Vorst JR, van de Velde CJH, Frangioni JV, Image-guided cancer surgery using near-infrared fluorescence, Nat. Rev. Clin. Oncol 10 (2013) 507–518, 10.1038/nrclinonc.2013.123. [PubMed: 23881033]

[14]. Manny TB, Patel M, Hemal AK, Fluorescence-enhanced robotic radical prostatectomy using real-time lymphangiography and tissue marking with percutaneous injection of unconjugated indocyanine green: The initial clinical experience in 50 patients, Eur. Urol 65 (2014) 1162–1168, 10.1016/j.eururo.2013.11.017. [PubMed: 24289911]

[15]. Jeschke S, Lusuardi L, Myatt A, Hruby S, Pirich C, Janetschek G, Visualisation of the lymph node pathway in real time by laparoscopic radioisotope- and fluorescence-guided sentinel lymph node dissection in prostate cancer staging, Urology 80 (2012) 1080–1087, 10.1016/j.urology.2012.05.050. [PubMed: 22990053]

[16]. Chennamsetty A, Zhumkhawala A, Tobis SB, Ruel N, Lau CS, Yamzon J, Wilson TG, Yuh BE, Lymph node fluorescence during robot-assisted radical prostatectomy with indocyanine green: prospective dosing analysis, Clin. Genitourin. Cancer 15 (2017) e529–e534, 10.1016/j.clgc.2016.10.014. [PubMed: 27939590]

[17]. Van Der Poel HG, Buckle T, Brouwer OR, Valdés Olmos RA, Van Leeuwen FWB, Intraoperative laparoscopic fluorescence guidance to the sentinel lymph node in prostate cancer patients:

clinical proof of concept of an integrated functional imaging approach using a multimodal tracer, Eur. Urol 60 (2011) 826–833, 10.1016/j.eururo.2011.03.024. [PubMed: 21458154]

[18]. Chen M, Yin M, Design and development of fluorescent nanostructures for bioimaging, Prog. Polym. Sci 39 (2014) 365–395, 10.1016/j.progpolymsci.2013.11.001.

[19]. Yang B, Zhang X, Zhang X, Huang Z, Wei Y, Tao L, Fabrication of aggregation-induced emission based fluorescent nanoparticles and their biological imaging application: recent progress and perspectives, Mater. Today 19 (2016) 284–291, 10.1016/j.mattod.2015.11.002.

[20]. Hill TK, Mohs AM, Image-guided tumor surgery: will there be a role for fluorescent nanoparticles?, Wiley Interdiscip Rev. Nanomedicine Nanobiotechnology 8 (2016) 498–511, 10.1002/wnan.1381. [PubMed: 26585556]

[21]. Laurent TC, Fraser JR, Hyaluronan, FASEB J. 6 (1992) 2397–2404, 10.1016/S0140-6736(01)35637-4. [PubMed: 1563592]

[22]. Jackson DG, The lymphatics revisited: new perspectives from the hyaluronan receptor LYVE-1, Trends Cardiovasc. Med 13 (2003) 1–7, 10.1016/S1050-1738(02)00189-5. [PubMed: 12554094]

[23]. Hill TK, Kelkar SS, Wojtynek NE, Souchek JJ, Payne WM, Stumpf K, Marini FC, Mohs AM, Near infrared fluorescent nanoparticles derived from hyaluronic acid improve tumor contrast for image-guided surgery, Theranostics 6 (2016) 2314–2328, 10.7150/thno.16514. [PubMed: 27877237]

[24]. Souchek JJ, Davis AL, Hill TK, Holmes MB, Qi B, Singh PK, Kridel SJ, Mohs AM, Combination treatment with orlistat-containing nanoparticles and taxanes is synergistic and enhances microtubule stability in taxane-resistant prostate cancer cells, Mol. Cancer Ther 16 (2017) 1819–1830, 10.1158/1535-7163.MCT-17-0013. [PubMed: 28615298]

[25]. Dosio F, Arpicco S, Stella B, Fattal E, Hyaluronic acid for anticancer drug and nucleic acid delivery, Adv. Drug Deliv. Rev 97 (2016) 204–236, 10.1016/j.addr.2015.11.011. [PubMed: 26592477]

[26]. Huang J, Zhang H, Yu Y, Chen Y, Wang D, Zhang G, Zhou G, Liu J, Sun Z, Sun D, Lu Y, Zhong Y, Biodegradable self-assembled nanoparticles of poly (d, llactide-co-glycolide)/hyaluronic acid block copolymers for target delivery of docetaxel to breast cancer, Biomaterials 35 (2014) 550–566, 10.1016/j.biomaterials.2013.09.089. [PubMed: 24135268]

[27]. Chen B, Miller RJ, Dhal PK, Hyaluronic acid-based drug conjugates: State-ofthe-art and perspectives, J. Biomed. Nanotechnol 10 (2014) 4–16, 10.1166/jbn.2014.1781. [PubMed: 24724495]

[28]. Saravanakumar G, Deepagan VG, Jayakumar R, Park JH, Hyaluronic acid-based conjugates for tumor-targeted drug delivery and imaging, J. Biomed. Nanotechnol 10 (2014) 17–31, 10.1166/jbn.2014.1761. [PubMed: 24724496]

[29]. Hill TK, Abdulahad A, Kelkar SS, Marini FC, Long TE, Provenzale JM, Mohs AM, Indocyanine green-loaded nanoparticles for image-guided tumor surgery, Bioconjug. Chem 26 (2015) 294–303, 10.1021/bc5005679. [PubMed: 25565445]

[30]. Kelkar SS, Hill TK, Marini FC, Mohs AM, Near infrared fluorescent nanoparticles based on hyaluronic acid: Self-assembly, optical properties, and cell interaction, Acta Biomater. 36 (2016) 112–121, 10.1016/j.actbio.2016.03.024. [PubMed: 26995504]

[31]. Hill TK, Davis AL, Wheeler FB, Kelkar SS, Freund EC, Lowther WT, Kridel SJ, Mohs AM, Development of a self-assembled nanoparticle formulation of orlistat, Nano-ORL, with increased cytotoxicity against human tumor cell lines, Mol. Pharm 13 (2016) 720–728, 10.1021/acs.molpharmaceut.5b00447. [PubMed: 26824142]

[32]. Qi B, Crawford AJ, Wojtynek NE, Holmes MB, Souchek JJ, Almeida-Porada G, Ly QP, Cohen SM, Hollingsworth MA, Mohs AM, Indocyanine green loaded hyaluronan-derived nanoparticles for fluorescence-enhanced surgical imaging of pancreatic cancer, Nanomedicine Nanotechnology, Biol. Med 14 (2018) 769–780, 10.1016/j.nano.2017.12.015.

[33]. Payne WM, Hill TK, Svechkarev D, Holmes MB, Sajja BR, Mohs AM, Multimodal imaging nanoparticles derived from hyaluronic acid for integrated preoperative and intraoperative cancer imaging Article ID 9616791, Contrast Media Mol. Imaging (2017), 10.1155/2017/9616791.

[34]. Mohs AM, Mancini MC, Provenzale JM, Saba CF, Cornell KK, Howerth EW, Nie S, An Integrated Widefield Imaging and Spectroscopy System for Contrast-Enhanced, Image-guided

Resection of Tumors, IEEE Trans. Biomed. Eng 62 (2015) 1416–1424, 10.1109/TBME.2015.2389626. [PubMed: 25585410]

[35]. Mattheolabakis G, Milane L, Singh A, Amiji MM, Hyaluronic acid targeting of CD44 for cancer therapy: from receptor biology to nanomedicine, J. Drug Target 23 (2015) 605–618, 10.3109/1061186X.2015.1052072. [PubMed: 26453158]

[36]. Yeh C-Y, Hsiao J-K, Wang Y-P, Lan C-H, Wu H-C, Peptide-conjugated nanoparticles for targeted imaging and therapy of prostate cancer, Biomaterials 99 (2016) 1–15, 10.1016/j.biomaterials.2016.05.015. [PubMed: 27209258]

[37]. Wolny PM, Banerji S, Gounou C, Brisson AR, Day AJ, Jackson DG, Richter RP, Analysis of CD44-hyaluronan interactions in an artificial membrane system: Insights into the distinct binding properties of high and low molecular weight hyaluronan, J. Biol. Chem 285 (2010) 30170–30180, 10.1074/jbc.M110.137562. [PubMed: 20663884]

[38]. Stevens JW, Palechek PL, Griebling TL, Midura RJ, Rokhlin OW, Cohen MB, Expression of CD44 isoforms in human prostate tumor cell lines, Prostate 28 (1996) 153–161, 10.1002/(SICI)1097-0045(199603)28:3<153::AID-PROS2>3.0.CO;2-G. [PubMed: 8628718]

[39]. Smith AM, Mancini MC, Nie S, Bioimaging: second window for in vivo imaging, Nat. Nanotechnol 4 (2009) 710–711, 10.1038/nnano.2009.326. [PubMed: 19898521]

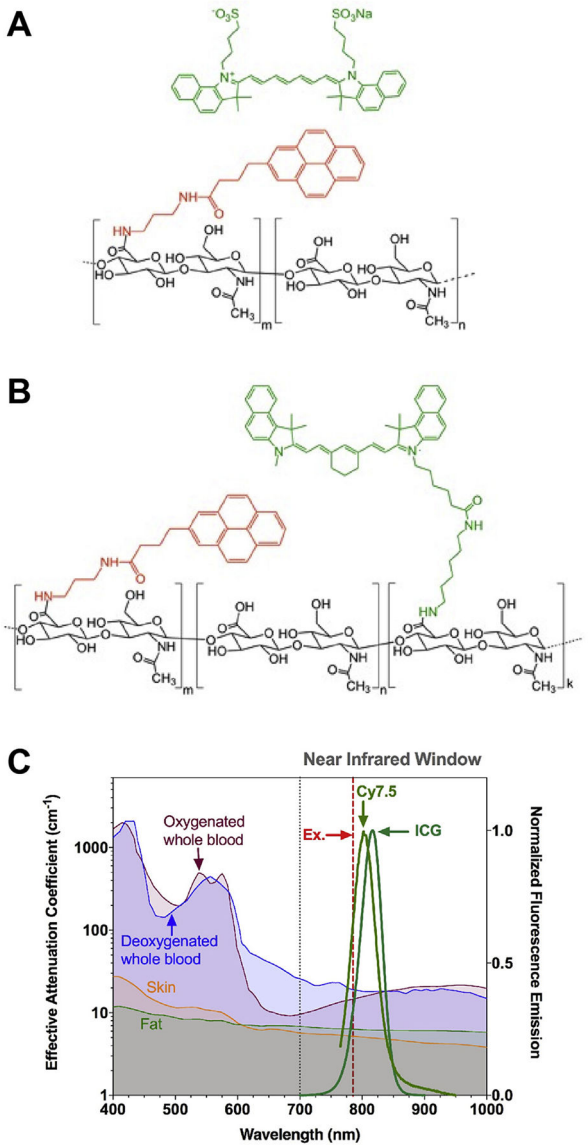

Fig. 1.

Structure of amphiphilic HA polymeric conjugates for NIR dye entrapment or conjugation. HA-PBA conjugates were synthesized with 10 kDa or 100 kDa HA polymers (black structure) conjugated with 10 wt% PBA (red structure). (A) ICG (green structure) was physically entrapped in HA-PBA, while (B) Cy7.5-amine (green structure) was conjugated to HA-PBA using EDC/NHS chemistry. Cy7.5, Cyanine7.5; ICG, indocyanine green; HA, hyaluronic acid; PBA, aminopropyl-1-pyrenebutanamide. (C) Normalized fluorescence of ICG and Cy7.5 compared to the effective attenuation coefficient spectra of relevant tissues [39]. Figure 1C is adapted by permission from Springer Nature: *Nature Nanotechnology*, Bioimaging: Second window for in vivo imaging, AM Smith, MC Mancini, S Nie, © 2009. (For interpretation of the references to colour in this figure legend, the reader is referred to the web version of this article.)

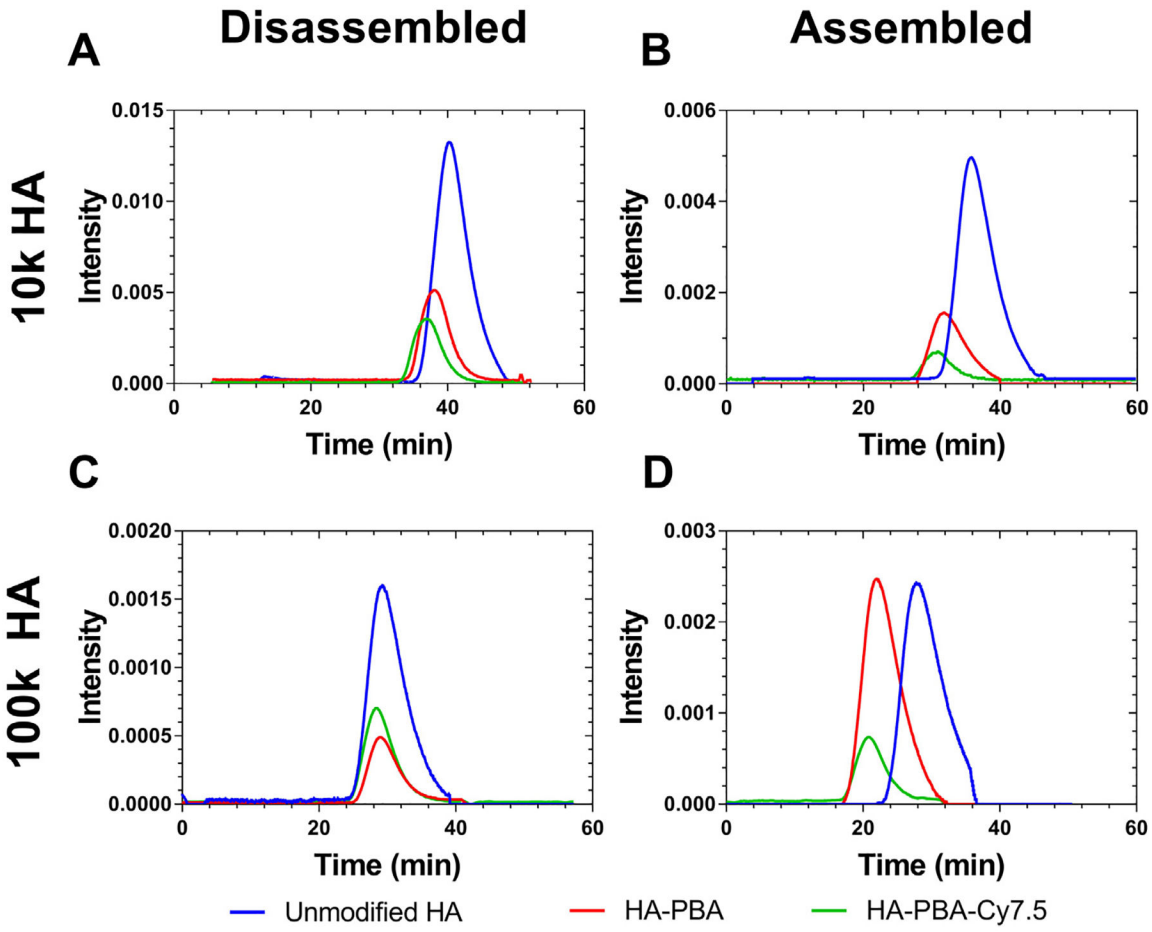

Fig. 2.

Size-exclusion chromatography of HA and HA conjugates reported as dRI spectra. Samples of HA, HA-PBA, and HA-PBA-Cy7.5 were prepared using either 10 kDa HA (A,B) or 100 kDa HA (C, D) and prepared in aqueous buffer (B, D) or 50:50 aqueous buffer DMSO ("disassembly buffer," A, C). (A) shows the difference between disassembled HA conjugates, comparing the difference in size between the three samples of 10 kDa HA. When compared to (B), which demonstrates the SEC profile of assembled conjugates, the samples appear slightly larger due to associations between polymer strands forming self-assembled nanoparticles. The same trend is observed for the 100 kDa HA samples, in which the assembled (D) samples are slightly larger than the disassembled (C) samples.

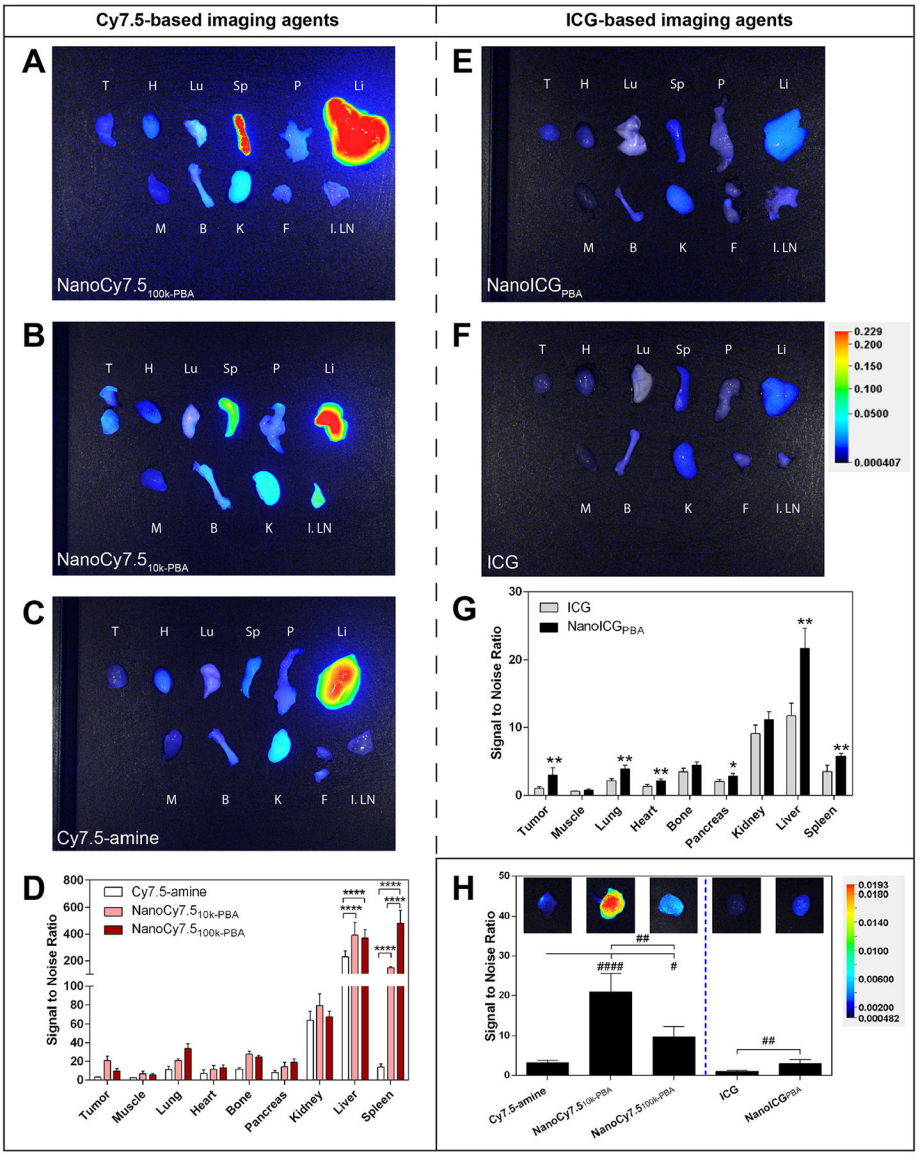

Fig. 3.

Biodistribution of contrast agents after administration in PC3 tumor-bearing nude mice. (A-C) Representative NIR fluorescence images of *ex vivo* organs harvested 24 h after intravenous administration of indicated contrast agent (1.2 nmol [984 ng] of Cy7.5/mouse for Cy7.5-amine, NanoCy7.5$_{10k\text{-}PBA}$, or NanoCy7.5$_{100k\text{-}PBA}$). All images are the “800 nm” channel overlaid onto the brightfield photograph from the Pearl Trilogy imaging system. Organ labels: T, tumor(s); H, heart; Lu, Lung; Sp, spleen; P, pancreas; Li, liver; M, muscle (i.e. quadriceps femoris muscle); B, bone (i.e. femur); K, kidney; F, fatty tissue adjacent to tumor with potential lymph; I. LN, inguinal lymph node with skin attached. (D) Quantitative summary of fluorescence intensity of organs collected 24 h after intravenous administration of the NanoCy7.5 conjugates and Cy7.5-amine control, where bars represent the average pixel signal-to-noise ratio (SNR; mean ± s.d) of N = 4 mice, with some tumors having two parts. $^{****}p < 0.0001$, two-way ANOVA with Tukey’s multiple comparisons test. (E, F)

Representative NIR fluorescence images of *ex vivo* organs harvested 24 h after intravenous administration of indicated contrast agent (10 nmol [7.75 μg] of ICG/mouse for ICG and $NanoICG_{PBA}$). (G) Quantitative summary of fluorescence intensity in the $NanoICG_{PBA}$ and ICG control groups, where bars represent the average pixel SNR (mean ± SD) of N = 3 mice for ICG and N = 4 mice for $NanoICG_{PBA}$, with some tumors having two parts. $^{*}p < 0.05$, $^{**}p < 0.01$, unpaired *t*-test. (H) The tumor SNR is shown with representative NIR fluorescence pictures of tumors scaled to the same level to better visualize the differences between groups, $^{\#}p < 0.05$, $^{\#\#}p < 0.01$, $^{\#\#\#\#}p < 0.0001$, one-way ANOVA with Tukey's multiple comparisons test for Cy7.5 groups, and $^{\#\#}p < 0.01$ Mann-Whitney test for ICG groups.

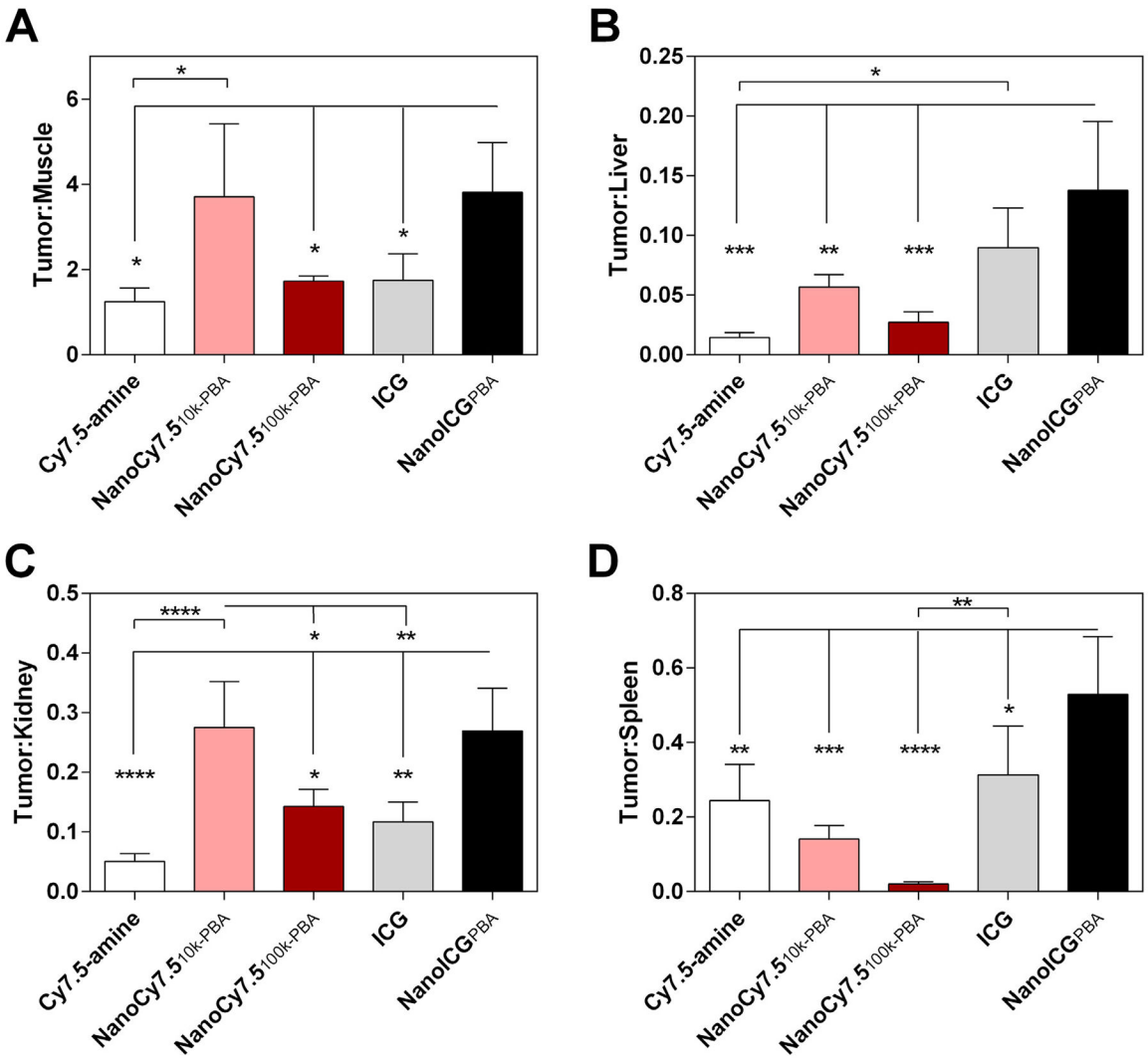

Fig. 4.

Tumor-to-organ ratios in PC3 tumor bearing nude mice. (A) Tumor-to-muscle, (B) tumor-to-liver, (C) tumor-to-kidney, and (D) tumor-to-spleen SNR ratios obtained from the *ex vivo* imaging in Fig. 2. *$p < 0.05$, **$p < 0.01$, ***$p < 0.001$, ****$p < 0.0001$ one-way ANOVA with Tukey's multiple comparisons test.

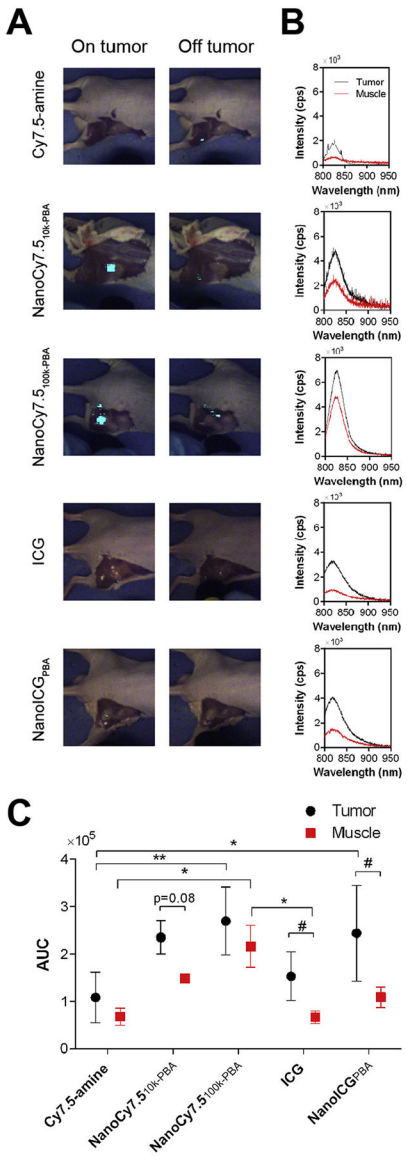

Fig. 5.

Image-guided surgery in mice bearing subcutaneous PC3 prostate tumors.(A) Surgical detection of tumors using FIGSS of representative mice 24 h after intravenous administration of indicated contrast agent (1.2 nmol of Cy7.5/mouse for Cy7.5-amine, NanoCy7.5$_{10k\text{-}PBA}$, or NanoCy7.5$_{100k\text{-}PBA}$; and 10 nmol of ICG/mouse for ICG and NanoICG$_{PBA}$). Images were taken when the laser was directed on the tumor and off the tumor. Simulated image-guided surgery was performed on n = 3 mice for ICG, and n = 4 mice for all other groups. (B) Spectroscopic signals from an excised tumor and muscle (ie quadriceps femoris muscle) of a representative mouse from each of the groups shown in (A). Integration time was 1 s for all groups, and excitation power was set to 30 mW for NanoCy7.5$_{10k\text{-}PBA}$ and 80 mW for all other groups. Curves were normalized to 80 mW excitation power. (C) Summary of spectroscopic signals of excised tumor and muscle based on AUC of the intensity vs. wavelength curves. Values are expressed as mean ± SD (n = 2

for NanoCy7.5$_{10k\text{-}PBA}$, n = 3 for ICG muscle, n = 4 for all other groups). *p < 0.05, **p < 0.01; as determined by two-way ANOVA with Tukey's method for multiple comparisons. #p < 0.05; as determined by unpaired *t*-test.

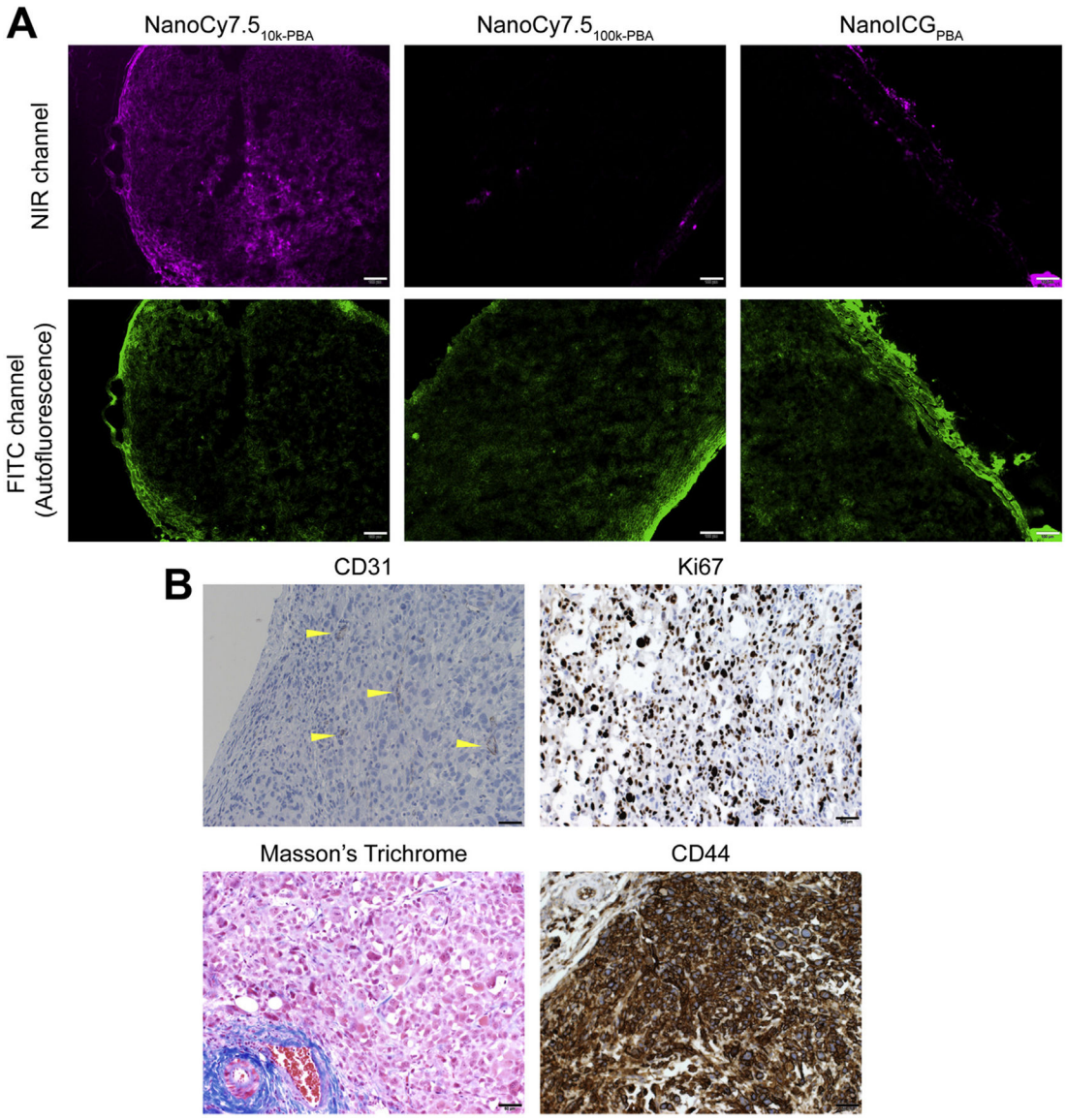

Fig. 6.

NIR dye distribution in tumors. (A) Representative fluorescence micrographs of tumors in the NIR channel after frozen sectioning for indicated NIR nanoparticles. Scale bar = 100 μm. (B) Representative tumor sections were stained with indicated dye (Masson's trichrome) or antibody (anti-mCD31, endothelial marker; anti-hKi67, proliferation marker; and anti-hCD44, a cell surface receptor for HA). Sections stained with antibodies (shown in brown) were counterstained with hematoxylin (shown in blue). CD31-positive vessels are marked with yellow arrowheads. Scale bar = 50 μm. (For interpretation of the references to colour in this figure legend, the reader is referred to the web version of this article.)

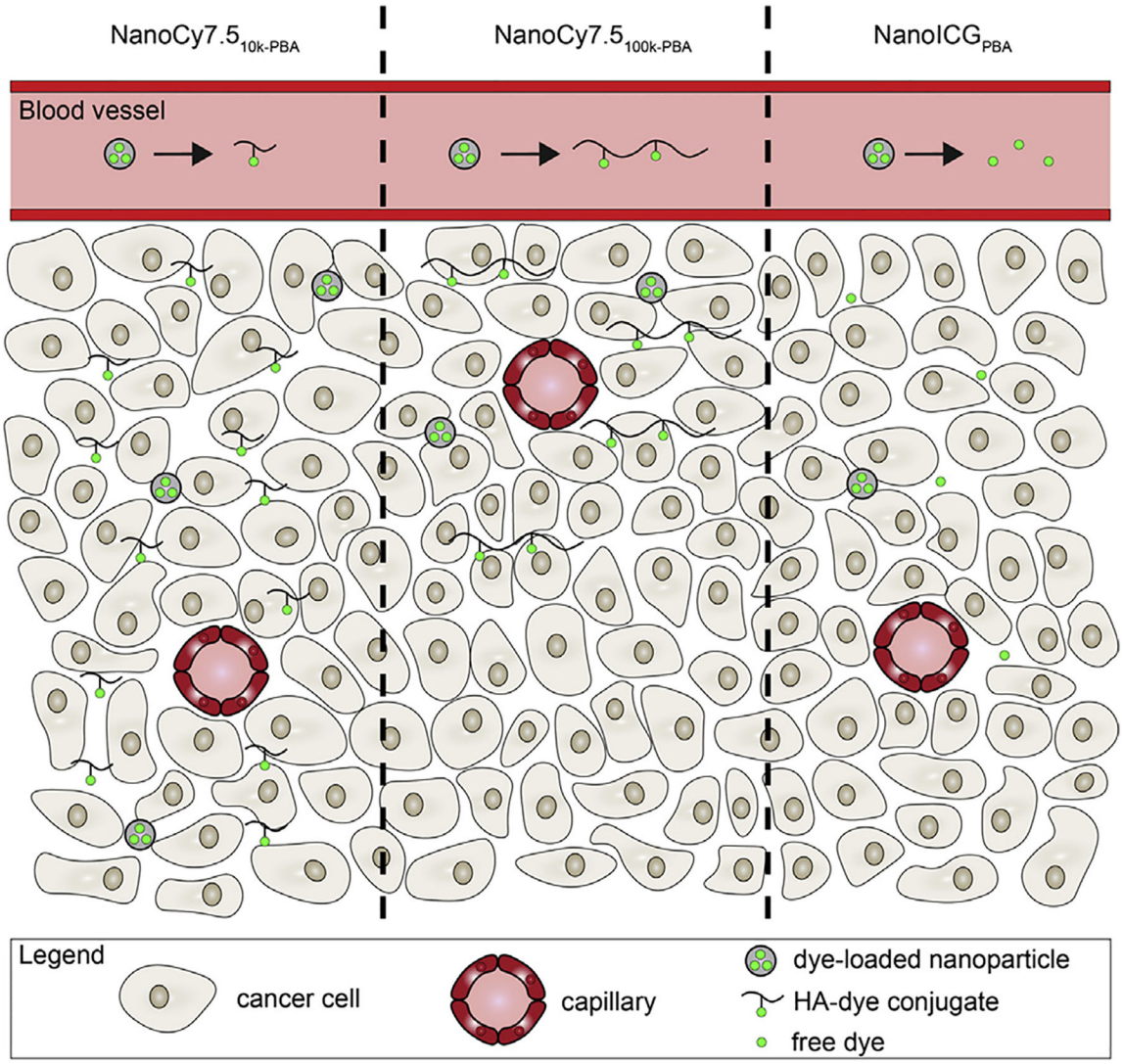

Fig. 7.

Summary of observations of nanoparticle-NIR dye distribution in tumors. Of the nanoparticles tested, NanoCy7.5$_{10k\text{-}PBA}$ with chemically-conjugated Cy7.5 had highest signal-to-noise ratio (SNR), high signal in image-guided surgery, and had NIR signal distributed throughout the tumor in microscopy. NanoCy7.5$_{100k\text{-}PBA}$ had increased SNR compared to free Cy7.5-amine, but had low tumor-to-organ distribution, had less contrast during image-guided surgery because of high signal in background tissue, and low tumor penetration. Since NanoICG$_{PBA}$ had physically entrapped ICG, we assume the dye is being released from the NP before getting to the tumor. NanoICG$_{PBA}$ had low SNR values, but because of low background tissue signal, had large tumor-to-organ distribution values, had dim but tumor-specific signal in image-guided surgery, and had low tumor penetration of released ICG. Nanoparticles are not drawn to scale.

Table 1

Summary of observations with NIR fluorescent nanoparticles tested.

Observation	Order
Biodistribution: Tumor Signal-to-Noise ratio	$NanoCy7.5_{10k\text{-}PBA}$ > $NanoCy7–5_{100k\text{-}PBA}$ > $NanolCG_{PBA}$
Biodistribution: Tumor-to-organ ratios	$NanolCG_{PBA}$ = $NanoCy7.5_{10k\text{-}PBA}$ > $NanoCy7.5_{100k\text{-}PBA}$
Image-guided surgery: brightness	$NanoCy7.5_{10k\text{-}PBA}$ = $NanoCy7.5_{100k\text{-}PBA}$ > $NanolCG_{PBA}$
Image-guided surgery: contrast	$NanoCy7.5_{10k\text{-}PBA}$ = $NanolCG_{PBA}$ > $NanoCy7.5_{100k\text{-}PBA}$